Method for detection and reconstruction of gravitational wave transients with networks of advanced detectors

S. Klimenko,[1] G. Vedovato,[2] M. Drago,[3] F. Salemi,[3] V. Tiwari,[1] G. A. Prodi,[4] C. Lazzaro,[2] K. Ackley,[1] S. Tiwari,[4,5] C. F. Da Silva,[1] and G. Mitselmakher[1]

[1]*University of Florida, P.O. Box 118440, Gainesville, Florida 32611, USA*
[2]*INFN, Sezione di Padova, via Marzolo 8, 35131 Padova, Italy*
[3]*Max Planck Institut für Gravitationsphysik, Callinstrasse 38, 30167 Hannover and Leibniz Universität Hannover, D-30167 Hannover, Germany*
[4]*University of Trento, Physics Department and INFN, Trento Institute for Fundamental Physics and Applications, via Sommarive 14, 38123 Povo, Trento, Italy*
[5]*Gran Sasso Science Institute (INFN), Via Francesco Crispi 7, I-67100 LAquila, Italy*

(Received 7 December 2015; published 11 February 2016)

We present a method for detection and reconstruction of the gravitational wave (GW) transients with the networks of advanced detectors. Originally designed to search for transients with the initial GW detectors, it uses significantly improved algorithms, which enhance both the low-latency searches with rapid localization of GW events for the electromagnetic follow-up and high confidence detection of a broad range of the transient GW sources. In this paper, we present the analytic framework of the method. Following a short description of the core analysis algorithms, we introduce a novel approach to the reconstruction of the GW polarization from a pattern of detector responses to a GW signal. This polarization pattern is a unique signature of an arbitrary GW signal that can be measured independently from the other source parameters. The polarization measurements enable rapid reconstruction of the GW waveforms, sky localization, and helps identification of the source origin.

DOI: 10.1103/PhysRevD.93.042004

I. INTRODUCTION

Advanced LIGO detectors [1] have started their operation at unprecedented sensitivity, targeting first detection of gravitational waves from astrophysical sources. A more robust detection of gravitational waves is anticipated in the next few years as the advanced LIGO reaches its designed sensitivity and the other advanced detectors Virgo [2], Kagra [3], and LIGO-India [4] come online. Numerous gravitational wave (GW) signals expected to be observed by the advanced detectors (∼40 binary neutron star and possible black hole mergers per year [5]) will begin our exploration of the gravitational wave sky and start the era of the gravitational wave astronomy.

The advanced detectors target the detection of GW transients for a wide range of promising astrophysical sources including various types of gamma-ray bursts, core-collapse supernovae, soft-gamma repeaters, cosmic strings, late inspiral and mergers of compact binaries, ringdowns of perturbed neutron stars or black holes, and as-yet-unknown systems. Most of these sources are difficult to model due to their complicated dynamics and because the equation of state of matter at neutron star densities is not known. Therefore, the search algorithms have been developed [6–9] for detection of GW transients or bursts of GW radiation in the detector bandwidth with no or little assumptions on the source models.

There are two different ways the GW searches are conducted: in real time and searches on the archived data. The objective of the real-time burst search is the identification and reconstruction of significant event candidates with low latency (within a few minutes). The reconstructed sky location can be promptly shared with the partner telescopes, which search for a coincident electromagnetic (EM) counterpart [10,11]. A prominent source for such joint observation is a merger of compact binary objects where one of the companions (or both) is a neutron star. Such mergers may produce several EM signals: gamma-ray busts (GRBs), GRB afterglow, kilonova, etc., which will fade away with the time scales ranging from seconds to days [12]. A small fraction of such mergers (when the GRB beam is pointing at us) can be independently detected by the gamma-ray telescopes and associated with a GW signal by the time of the event. However, most of the compact binary mergers require a prompt sky localization with the GW detectors and follow-up EM searches for possible afterglow. Similar observations can be performed for the galactic events such as supernovae or soft-gamma repeaters, which may produce both the EM and neutrino counterparts. On the contrary, the objective of the archived burst analysis is to establish a significance of observed events and identify their progenitors. Such analysis requires detail background studies and accurate reconstruction of the source parameters, which may not be readily available with low latency.

Both types of searches and the sky localization studies have been performed with the baseline burst algorithm

Coherent WaveBurst (CWB) [6] used in the analysis of data from the initial instruments [13–18]. In this paper, we describe the improvements of the CWB algorithm, which is currently used both for the real-time burst search and several archived searches with the networks of advanced detectors. This second-generation CWB algorithm includes several novelties. The time-frequency analysis has been updated with a novel time-frequency transform [19], which improved the waveform reconstruction. It also significantly improved the computational performance of the algorithm, enabling a robust low-latency operation. The data conditioning (whitening, removal of the spectral artifacts, etc.) has been enhanced with the data regression algorithms [20]. Fast reconstruction of the chirp mass [21] has been introduced to enable rapid identification of the compact binary coalescence sources. The extensive sky localization studies have been performed [22].

In this paper, we focus on the CWB analytic framework enhanced with a novel method for reconstruction of the GW polarization from the pattern of detector responses to a GW signal. It significantly simplifies the solution of the inverse problem in the burst analysis and enables weakly modeled burst searches with the polarization constraints.

The paper is organized as follows. Section II gives introduction into the coherent network analysis required to introduce in Sec. III the dual stream likelihood analysis and the polarization pattern. In Sec. IV we describe how it can be used to construct network regulators—the model-independent constraints used in the CWB analysis.

II. OVERVIEW

Data from a network of K detectors are presented as discrete series $x_k[i]$ in the most general time-frequency (TF) domain, where k is the detector index in the network, and i is the data sampling (TF pixel) index. The real TF series $x_k[i]$ is obtained from the detector time series with the Wilson-Daubechies-Meyer (WDM) transform [19]. The data are conditioned to remove spectral features, such as violin, power, and mechanical lines [20].

A detector noise (assuming to be Gaussian) is described by the WDM power spectral density $S_k[i]$ estimated for every data sample. Therefore, $S_k[i]$ is a TF series as well, which is convenient for the characterization of a quasistationary noise typical for real detectors. The noise-scaled (whitened) data are defined as $w_k[i] = x_k[i]/\sqrt{S_k[i]}$.

The whitened TS series from all detectors are combined to obtain the energy TF maps $E[i] = \sum_k w_k^2[i]$, where $E[i]$ are maximized over all possible time-of-flight delays in the network. The energy maps are used to identify TF areas (cluster C, $i \in C$) with the excess energy above the baseline detector noise. The TF clusters identified with an appropriate clustering algorithm define the burst events, which are analyzed to extract the signal waveform, polarization, and sky location (inverse problem).

A. Formulation of the inverse problem for bursts

The data vector $\mathbf{x}[i] = \{x_1[i], \ldots, x_K[i]\}$ recorded by a network of GW detectors at the time of a gravitational wave signal $\mathbf{h}[i] = [h_+[i], h_\times[i]]$ with the source sky location at θ and ϕ is a superposition of the network response $\mathcal{F}\mathbf{h}[i]$ and noise $\mathbf{n}[i]$:

$$\mathbf{x}[i] = \mathcal{F}\mathbf{h}[i] + \mathbf{n}[i], \tag{2.1}$$

where the h_+ and $h_\times$ are the amplitudes of the two GW polarization components, and $\mathcal{F}$ is the network antenna pattern matrix

$$\mathcal{F} = \begin{bmatrix} F_{1+}(\theta,\phi) & F_{1\times}(\theta,\phi) \\ \cdots & \cdots \\ F_{K+}(\theta,\phi) & F_{K\times}(\theta,\phi) \end{bmatrix}. \tag{2.2}$$

The antenna patterns often include a transformation by the polarization angle Ψ. But this transformation is equivalent to a rotation of the wave frame where the vector $\mathbf{h}$ is defined. The network response is Ψ invariant, and, therefore, the polarization angle can be included in the definition of $\mathbf{h}$.

To solve the inverse problem, one should find the amplitudes of the GW polarization components $(h_+, h_\times)$ and the sky coordinates (θ, ϕ) from a coincident output of several GW detectors. Initially, this problem was considered by Gürsel and Tinto [23] for a network of three detectors. A more solid statistical foundation of the problem was presented by Flanagan and Hughes [24], who considered a likelihood method for the estimation of the signal parameters. They define the likelihood ratio

$$\Lambda(\mathbf{x}, \Omega) = \frac{p(\mathbf{x}|\mathbf{h}(\Omega))}{p(\mathbf{x}|0)}, \tag{2.3}$$

where Ω is a parameter set describing the signal, the $p(\mathbf{x}|0)$ is the joint probability that the data are only instrumental noise, and $p(\mathbf{x}|\mathbf{h})$ is the joint probability that a GW signal $\mathbf{h}$ is present in the data $\mathbf{x}$. The sample index i is omitted to stress that $i \in C$, where C is a collection of the TF pixels (cluster).

The explicit form of the likelihood ratio is determined by the noise model $p(\mathbf{x}|0)$ and by the signal model $\mathbf{h}(\Omega)$. For unmodeled burst signals, $\Omega = (h_+, h_\times, \theta, \phi)$, which can be found by analytical or numerical variation of Λ. The advantage of the likelihood method is that it allows introduction of the signal and noise models and can be applied to an arbitrary detector network.

B. Unconstrained likelihood analysis

This section presents the solution of the inverse problem assuming that the burst parameter set Ω is not constrained by a source model, and the noise of detectors in the network

is quasistationary and Gaussian with the power spectral densities $S_1, \ldots, S_K$. The noise-scaled data vector is then

$$\mathbf{w}[i] = \frac{x_1[i, \tau_1(\theta,\phi)]}{\sqrt{S_1[i]}}, \ldots, \frac{x_K[i, \tau_K(\theta,\phi)]}{\sqrt{S_K[i]}}, \tag{2.4}$$

where the detector amplitudes $x_k[i, \tau_k(\theta,\phi)]$ take into account the time-of-flight delays τ_k depending upon the source coordinates θ and ϕ. Respectively, the noise-scaled network response vector is

$$\boldsymbol{\xi}[i] = \mathbf{F}[i]\mathbf{h}[i], \tag{2.5}$$

where $\mathbf{F}[i]$ is the noise-scaled antenna pattern matrix

$$\mathbf{F}[i] = \begin{bmatrix} \frac{F_{1+}(\theta,\phi)}{\sqrt{S_1[i]}} & \frac{F_{1\times}(\theta,\phi)}{\sqrt{S_1[i]}} \\ \cdots & \cdots \\ \frac{F_{K+}(\theta,\phi)}{\sqrt{S_K[i]}} & \frac{F_{K\times}(\theta,\phi)}{\sqrt{S_K[i]}} \end{bmatrix}. \tag{2.6}$$

We also introduce the network matrix $\mathbf{f}$, which is obtained from $\mathbf{F}$ by the transformation to the dominant polarization frame (DPF) introduced by Klimenko *et al.* [25].

The likelihood functional $\mathcal{L}$ is defined as twice the logarithm of the likelihood ratio Λ,

$$\mathcal{L}[\mathbf{h}] = 2(\mathbf{w}|\boldsymbol{\xi}) - (\boldsymbol{\xi}|\boldsymbol{\xi}), \tag{2.7}$$

where the inner products $(\mathbf{w}|\boldsymbol{\xi})$ and $(\boldsymbol{\xi}|\boldsymbol{\xi})$ are calculated over the TF cluster.

The solution for the GW waveforms $\mathbf{h}$ is found by variation of the likelihood functional $\mathscr{L}[\mathbf{h}]$. It is convenient to introduce the antenna pattern vectors $\mathbf{f}_+$ and $\mathbf{f}_\times$, which are simply the columns of the matrix $\mathbf{f}$ and satisfy the DPF conventions: $(\mathbf{f}_+ \cdot \mathbf{f}_\times) = 0$ and $|\mathbf{f}_\times| \le |\mathbf{f}_+|$. These two vectors define a network plane where the GW response vector $\boldsymbol{\xi}$ must be located. The likelihood variation gives a system of linear equations for the amplitudes $h_+[i]$ and $h_\times[i]$ (also defined in the DPF)

$$\begin{bmatrix} (\mathbf{w}[\mathbf{i}] \cdot \mathbf{e}_+[i]) \\ (\mathbf{w}[\mathbf{i}] \cdot \mathbf{e}_\times[i]) \end{bmatrix} = \begin{bmatrix} |\mathbf{f}_+[i]| & 0 \\ 0 & |\mathbf{f}_\times[i]| \end{bmatrix} \begin{bmatrix} h_+[i] \\ h_\times[i] \end{bmatrix}, \tag{2.8}$$

where $\mathbf{e}_+$ and $\mathbf{e}_\times$ are the unit vectors along $\mathbf{f}_+$ and $\mathbf{f}_\times$, respectively. Note, the 2×2 matrix in Eq. (2.8) characterizes the network sensitivity to the two GW polarizations. The maximum likelihood ratio statistic is calculated by substituting the solutions into $\mathcal{L}[\mathbf{h}]$. The result can be written as

$$L_{\max} = \sum_{i \in C} \mathbf{w}[i] P[i] \mathbf{w}^T[i], \tag{2.9}$$

where the matrix P is the projection constructed from the components of the unit vectors $\mathbf{e}_+$ and $\mathbf{e}_\times$:

$$P_{nm}[i] = e_{n+}[i] e_{m+}[i] + e_{n\times}[i] e_{m\times}[i]. \tag{2.10}$$

The kernel of the projection P is the network plane defined by these two vectors. The null space of the projection P defines the residual detector noise, which is referred to as the null stream.

C. Reconstructed network response

The maximum likelihood ratio statistic $L_{\max}$ is a quadratic form [see Eq. (2.9)], which can be split into the incoherent E_i and coherent E_c parts

$$E_i = \sum_{i \in C} \sum_n w_n[i] P_{nn}[i] w_n[i], \tag{2.11}$$

$$E_c = \sum_{i \in C} \sum_{n \ne m} w_n[i] P_{nm}[i] w_m[i]. \tag{2.12}$$

These coherent statistics, together with the energy of the null stream E_n, are widely used in the burst searches for the construction of the event selection cuts. For example, the network correlation coefficient [6]

$$c_c = E_c / (|E_c| + E_n) \tag{2.13}$$

provides a powerful event consistency test to distinguish genuine GW events ($c_c \sim 1$) from spurious events ($c_c \ll 1$) produced by the detectors. The statistic E_c (coherent energy) is particularly important because it depends on the cross-correlation terms between the detector pairs. It is used for the construction of the burst detection statistic

$$\eta_c = (c_c E_c K/(K-1))^{1/2}, \tag{2.14}$$

which is an estimator of the network coherent signal-to-noise ratio for correlated GW signals recorded by different detectors.

The coherent statistics are very beneficial for the burst analysis, provided they are correctly constructed to address the "two-detector paradox" [26]. Namely, for any network of two detectors, the cross terms of the projection operator $P_{nm}[i]$ [Eq. (2.10)] are always equal to zero, or $E_c = 0$. Clearly, for two coaligned detectors with the identical detector responses, this is not true, which constitutes the two-detector paradox.

The origin of the two-detector paradox is the ambiguity of the projection operator. The likelihood $L_{\max}$ is invariant with respect to the rotation in the network plane where any two orthogonal unit vectors can be used for the construction of the projection $P_{nm}[i]$. Therefore, we select two such unit vectors $\mathbf{u}[i]$ and $\mathbf{v}[i]$ that the likelihood component corresponding to the vector $\mathbf{v}[i]$ vanishes, and the projection $P_{nm}(\mathbf{v}[i])$ can be omitted. The $L_{\max}$ and the coherent statistics are given by the projection

$$P_{nm}(\mathbf{u}[i]) = u_n[i] u_m[i], \tag{2.15}$$

which resolves the two-detector paradox. The vectors $\mathbf{u}[i]$ define the reconstructed network response

$$\boldsymbol{\xi}_r[i] = (\mathbf{w}[i] \cdot \mathbf{u}[i])\mathbf{u}[i], \tag{2.16}$$

whose components are the unconstrained likelihood estimators of the noise-scaled detector responses.

III. DUAL STREAM LIKELIHOOD ANALYSIS

As defined in Sec. II, a network noise-scaled data stream is $\mathbf{w}$. Additionally, a quadrature data stream $\tilde{\mathbf{w}}$ is used. It can be obtained from the original detector data, which is phase shifted by $-90°$. The data $(\mathbf{w}, \tilde{\mathbf{w}})$ define the network dual data stream conveniently provided by the WDM transform: applied to the detector time series, it generates both data streams. For the unmodeled reconstruction (see Sec. II B), the analysis can be performed individually for each data stream resulting in the likelihood statistics $L_{\max}$ and $\tilde{L}_{\max}$. Formally, the quadrature data stream does not contain any new information, nevertheless, $L_{\max} \neq \tilde{L}_{\max}$. This is because for a given time-frequency cluster, the quadrature counterparts may have different contributions both from the signal and noise. Therefore, the inclusion of the quadrature stream can improve the collection of the signal energy and, respectively, improve the reconstruction. Also, the dual data stream is required for the inclusion of the signal polarization models into the analysis.

A. Phase transformation

Each dual data stream sample is presented by the data vectors $\mathbf{w}[i]$ and $\tilde{\mathbf{w}}[i]$. We define a phase transformation to calculate the amplitudes for an arbitrary phase shift λ_i:

$$\mathbf{w}'[\mathbf{i}] = \mathbf{w}[\mathbf{i}] \cos\lambda_{\mathbf{i}} + \tilde{\mathbf{w}}[\mathbf{i}] \sin\lambda_{\mathbf{i}}, \tag{3.1}$$

$$\tilde{\mathbf{w}}'[\mathbf{i}] = \tilde{\mathbf{w}}[\mathbf{i}] \cos\lambda_{\mathbf{i}} - \mathbf{w}[\mathbf{i}] \sin\lambda_{\mathbf{i}}, \tag{3.2}$$

where the individual phase shift λ_i is applied to each data sample. In the likelihood functional, the same transformation should be applied to the detector responses $\boldsymbol{\xi}[i]$ and $\tilde{\boldsymbol{\xi}}[i]$. The quadrature likelihood functionals $\mathcal{L}$ and $\tilde{\mathcal{L}}$,

$$\mathcal{L}[\mathbf{h}] = 2(\mathbf{w}|\boldsymbol{\xi}) - (\boldsymbol{\xi}|\boldsymbol{\xi}), \tag{3.3}$$

$$\tilde{\mathcal{L}}[\mathbf{h}] = 2(\tilde{\mathbf{w}}|\tilde{\boldsymbol{\xi}}) - (\tilde{\boldsymbol{\xi}}|\tilde{\boldsymbol{\xi}}) \tag{3.4}$$

vary as the phase transformation is applied; however, the total likelihood $\mathcal{L}_\circ = \mathcal{L} + \tilde{\mathcal{L}}$ is the phase invariant. There are several distinct phase transformations, two of which are considered below.

In the orthogonal phase transformation (OPT), the phase shift is selected such that the network responses $\boldsymbol{\xi}'[i]$ and $\tilde{\boldsymbol{\xi}}'[i]$ in the network plane become orthogonal to each other. The OPT pattern is used for calculation of dual stream coherent statistics in Sec. IV A.

The polarization phase transformation (PPT) is defined by the scalar products of the network response and the antenna pattern vectors

$$\cos\lambda_i \propto (\boldsymbol{\xi}[i] \cdot \mathbf{e}_+[i]), \qquad \sin\lambda_i \propto (\tilde{\boldsymbol{\xi}}[i] \cdot \mathbf{e}_+[i]). \tag{3.5}$$

The purpose of the phase transformations is to obtain the signal polarization patterns. Namely, the wave polarization is captured by the network as a distinct pattern of the GW responses in the network plane, which is revealed when a particular phase transformation is applied.

B. Polarization pattern

To describe the polarization state of a generic GW signal, the following parametrization of the wave is used:

$$\boldsymbol{\xi} = h\mathbf{F}_+(\psi) + eH\mathbf{F}_\times(\psi), \tag{3.6}$$

$$\tilde{\boldsymbol{\xi}} = -H\mathbf{F}_+(\psi) + eh\mathbf{F}_\times(\psi), \tag{3.7}$$

where the instantaneous parameters of the signal are as follows: h and H are the strain amplitudes, ψ is the polarization angle, and e is the wave ellipticity. Here and below in the text, we omit the sample index i. In general, these are the *ad hoc* wave parameters; however, they can be related to the astrophysical wave parameters as described in Sec. III C. For this particular convention, the $\boldsymbol{\xi}$ and $\tilde{\boldsymbol{\xi}}$ are the $0°$-phase and $-90°$-phase network responses, and the sign of e defines the wave chirality or the sign of the quadruple product $[\boldsymbol{\xi} \times \tilde{\boldsymbol{\xi}}] \cdot [\mathbf{F}_+(\psi) \times \mathbf{F}_\times(\psi)]$. The antenna pattern vectors $\mathbf{F}_+(\psi)$ and $\mathbf{F}_\times(\psi)$ are related to the DPF vectors $\mathbf{f}_+$ and $\mathbf{f}_\times$,

$$\mathbf{F}_+(\psi) = \mathbf{f}_+ \cos(\gamma) - \mathbf{f}_\times \sin(\gamma), \tag{3.8}$$

$$\mathbf{F}_\times(\psi) = \mathbf{f}_\times \cos(\gamma) + \mathbf{f}_+ \sin(\gamma), \tag{3.9}$$

where $\gamma = \Psi - \psi$, and Ψ is the DPF angle. The PPT pattern is obtained by application of the transformation (3.5) to the vectors $(\boldsymbol{\xi}, \tilde{\boldsymbol{\xi}})$ (3.6) and (3.7). The resulting PPT pattern is described by the following tree vectors oriented along the $\mathbf{f}_+$ and $\mathbf{f}_\times$:

$$\boldsymbol{\xi}_+ = \mathbf{f}_+ h_\circ \beta_+(e,\gamma), \tag{3.10}$$

$$\boldsymbol{\xi}_\times = -\mathbf{f}_\times h_\circ \frac{1-e^2}{2} \sin(2\gamma)\beta_+^{-1}(e,\gamma), \tag{3.11}$$

$$\tilde{\boldsymbol{\xi}}_\times = \mathbf{f}_\times e h_\circ \beta_+^{-1}(e,\gamma), \tag{3.12}$$

where $h_\circ = \sqrt{h^2 + H^2}$ is the wave amplitude and

$$\beta_{\pm}(e,\gamma) = \frac{1}{\sqrt{2}}[1 + e^2 \pm (1 - e^2)\cos(2\gamma)]^{1/2}. \quad (3.13)$$

The product $h_{\circ}\beta_{+}(e,\gamma)$ is the norm of $\sin(\lambda_i)$ and $\cos(\lambda_i)$ in Eq. (3.5). The vectors $\boldsymbol{\xi}_{+}$ and $\boldsymbol{\xi}_{\times}$ describe the 0°-phase network response, and the vector $\tilde{\boldsymbol{\xi}}_{\times}$ describes the −90°-phase network response. By measuring these three vectors for each network data sample, the instantaneous signal parameters h_o, e, and ψ can be determined.

For a given GW event, the collection of vectors $\{\boldsymbol{\xi}_{+}, \boldsymbol{\xi}_{\times}, \tilde{\boldsymbol{\xi}}_{\times}\}$ describes its unique polarization pattern. Figure 1 shows the examples of the polarization patterns. However, this pattern can be significantly distorted by the network. For example, the detector noise adds random vectors to the GW responses and randomizes the polarization patterns for a weak GW signal. Also, the measured polarization pattern strongly depends on the network alignment factor: $\alpha = |\mathbf{f}_{\times}|/|\mathbf{f}_{+}|$. For any practical network $\alpha < 1$; therefore, the polarization pattern is always distorted (biased) by the network. The bias correction is straightforward; however, it becomes increasingly inaccurate when $\alpha \ll 1$. When $\alpha = 0$, only the $\boldsymbol{\xi}_{+}$ vector can be measured regardless of what the GW polarization state is. Namely, the original GW polarization cannot be reconstructed from such pattern of the network responses. The network of LIGO detectors has $\alpha \ll 1$ for a significant fraction of the sky (see top of Fig. 2).

Therefore, in most cases the polarization state of a GW signal cannot be measured. To improve the polarization coverage, one has to increase the alignment factor by adding more detectors to the network with optimally oriented detector arms (see bottom of Fig. 2). The full polarization coverage is achieved when α is close to unity, which greatly improves and simplifies the reconstruction. In this case, the polarization state of an arbitrary GW signal can be unambiguously identified from the pattern of the network responses in the network plane. Also, a more complete polarization coverage helps reconstruction of the sky coordinates and other source parameters.

C. Polarization constraints

The wave parameters $e[i]$ and $\psi[i]$ describe the polarization pattern. In some cases, they can be related to the astrophysical source parameters. In this section, we explicitly use the sample index i to demonstrate that the event parameter may vary during its time-frequency evolution. For example, for binary systems, $e[i]$ are defined by the inclination angle of the source, and $\psi[i]$ are defined by the polarization angle. The parameters $e[i]$ and $\psi[i]$ can be constrained when sources with a certain polarization state are considered. For unmodeled signals, all $e[i]$ and $\psi[i]$ are free parameters, or, in other words, the wave polarization is random (r waves). In this case, the solution for the network responses has been already described in the previous section. By imposing constraints on $e[i]$ and $\psi[i]$, the r waves can be divided into subclasses with more definite polarization states. For example, most GW signals should produce patterns with fixed chirality (all $e[i] > 0$ or all $e[i] < 0$). Therefore, the vectors $\tilde{\boldsymbol{\xi}}_{\times}$ can be constrained to

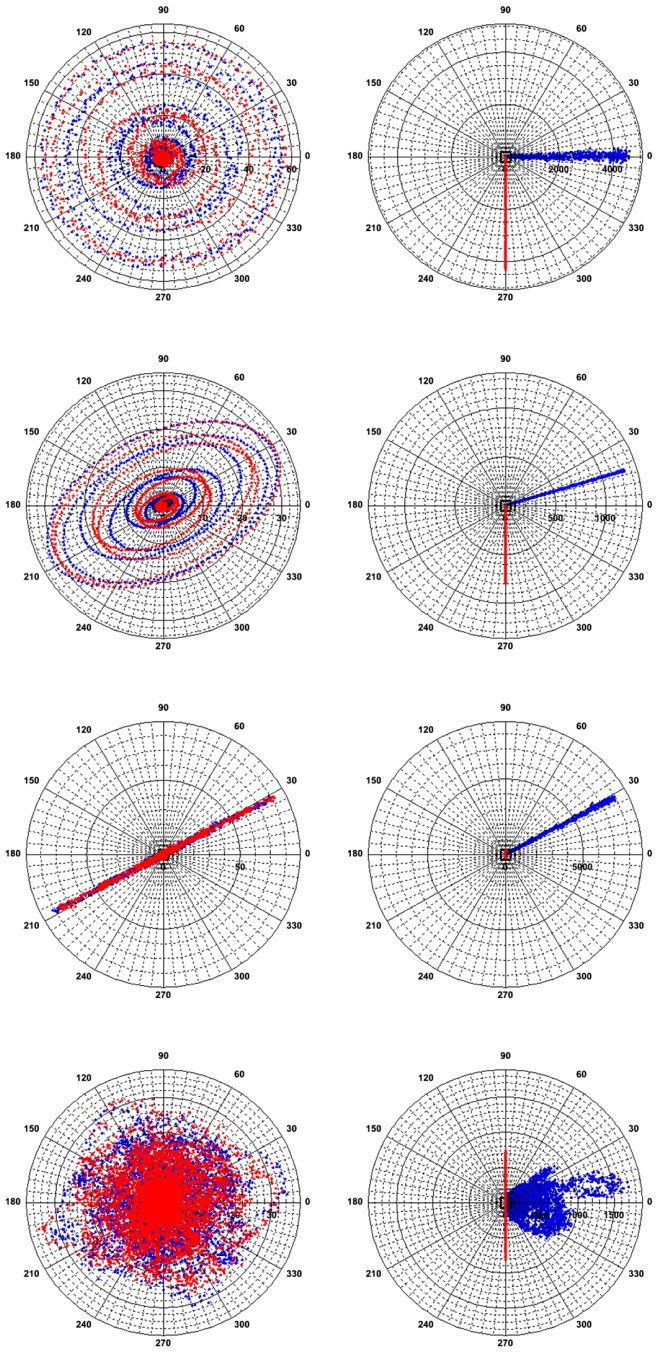

FIG. 1. Polarization patterns (from top to bottom) for waves with circular, elliptical, linear, and random polarization, before (left plots) and after (right plots) the PPT is applied. Dots of two different colors represent the orientation and amplitude of the 0°-phase (blue) and −90°-phase (red) response vectors originating at zero. The network antenna vectors form the coordinate frame with $\mathbf{f}_{\times}$ and $\mathbf{f}_{+}$ pointing along the vertical and horizontal axis, respectively. The patterns are calculated for a sky location where $|\mathbf{f}_{\times}| \approx |\mathbf{f}_{+}|$.

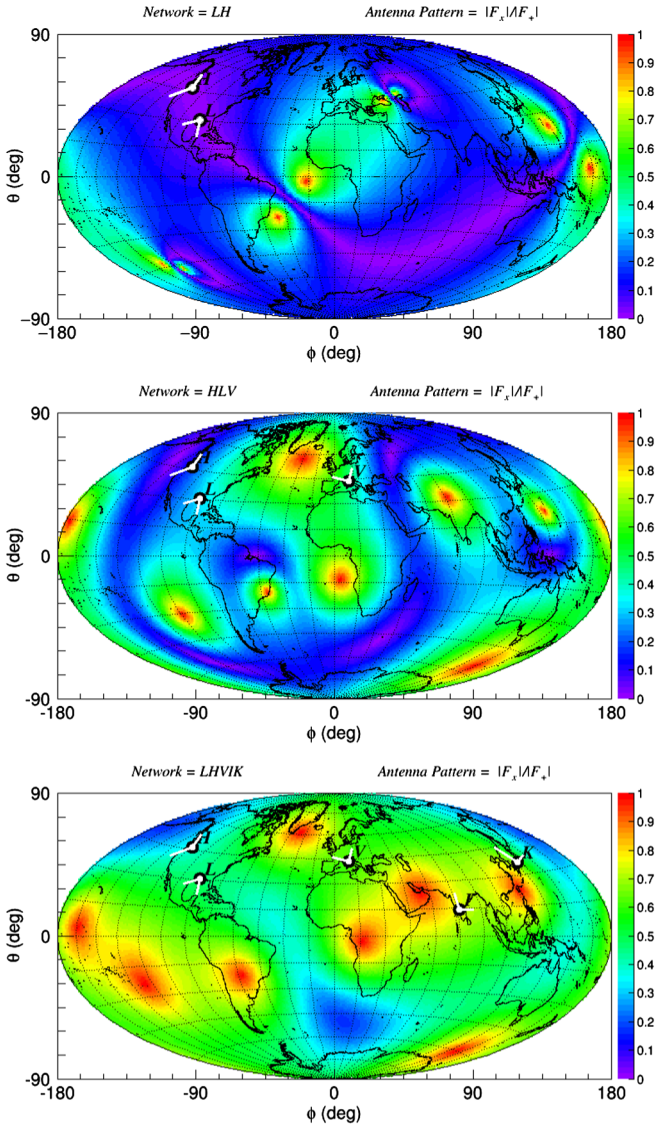

FIG. 2. The distribution of α over the sky for the Livingston-Hanford network (top), Livingston-Hanford-Virgo (middle), and Livingston-Hanford-Virgo-LIGO-India-Kagra (bottom). The detector site locations and the orientations of the arms are shown on the map. The LIGO-India location is just an example: there is no official site yet.

have the same chirality (ι waves). A more narrow subclass of ι waves is nonprecessing binary systems, where the parameters $e[i]$ are related to the inclination angle of the source and, therefore, $e[i] = \text{const}$. The angles $\psi[i]$ define the orientation of the reconstructed response vectors in the network plane. Assuming that the parameters $e[i]$ are free, the constraint $\psi[i] = \text{const}$ describes a particular class of GW signals with the same direction of the network response vectors (Ψ waves). The elliptical, linear, and circular waves are defined when both angles $e[i]$ and $\psi[i]$ are constrained. The constraints for the ι waves and Ψ waves and their combinations characterizing different polarization models are summarized in Table I.

The simplest solution is for the waves with the circular polarization: $e[i] = \pm 1$. A less strict (loose) circular polarization constraint is when $\boldsymbol{\xi}_\times = 0$. In this case, the network responses are defined by the vectors $\boldsymbol{\xi}_+$ and $\tilde{\boldsymbol{\xi}}_\times$, and the condition $e[i] = \pm 1$ is not enforced. For linear waves, $e[i] = 0$ and all 0°-phase response vectors are coaligned, or $\psi[i] = \text{const}$. Respectively, a less strict (loose) linear polarization constraint is defined by the condition $\tilde{\boldsymbol{\xi}}_\times = 0$ when the condition $\psi[i] = \text{const}$ is not enforced. The polarization constraints can be used to construct weakly modeled burst searches targeting broad classes of GW transients. The ι-wave constraint can be applied to any rotating source. The elliptical, circular, and the ψ-wave constraints can be used to search for compact binary sources with different spin configurations.

D. Likelihood solutions

The solution for the wave parameters $h_\circ$, e, and ψ, and, hence, the waveforms $\boldsymbol{\xi}$ and $\tilde{\boldsymbol{\xi}}$, can be obtained by maximizing the likelihood functional in Eqs. (3.3) and (3.4). For the unconstraints case when all the wave parameters are free, it is straightforward to show that the solutions for the network responses are given by the projections of the data vectors $(\mathbf{w}, \tilde{\mathbf{w}})$ on the network plane. As described above, the unmodeled burst analysis can be constrained to search for GW signals with various polarization states. In the general case, the constrained likelihood problem is hard to solve analytically, and the numerical solutions are computationally prohibitive. To solve this problem, we apply the phase transformation in Eq. (3.5) to the data vectors $\mathbf{w}$ and $\tilde{\mathbf{w}}$. This transformation reveals the underlying polarization pattern $\{\mathbf{w}_+, \mathbf{w}_\times, \tilde{\mathbf{w}}_\times\}$ smeared by the detector noise. The detector responses can be reconstructed directly from this pattern. The solutions for different polarization states can be obtained by imposing the polarization constraints in Table I. As follows from Eqs. (3.10)–(3.12), for linear ($e = 0$) and circular ($e \pm 1$) waves, the components $\tilde{\boldsymbol{\xi}}_\times = 0$ and $\boldsymbol{\xi}_\times = 0$, respectively. Therefore, the reconstructed responses for the loose linear polarization constraint are $(\boldsymbol{\xi}_+ = \mathbf{w}_+,\ \boldsymbol{\xi}_\times = \mathbf{w}_\times,\ \tilde{\boldsymbol{\xi}}_\times = 0)$ and for the loose circular polarization constraint they are $(\boldsymbol{\xi}_+ = \mathbf{w}_+, \boldsymbol{\xi}_\times = 0, \tilde{\boldsymbol{\xi}}_\times = \tilde{\mathbf{w}}_\times)$. The solution for linear waves is $(\boldsymbol{\xi}_+ = \mathbf{p}_+,\ \boldsymbol{\xi}_\times = \mathbf{p}_\times,\ \tilde{\boldsymbol{\xi}}_\times = 0)$, where the $\mathbf{p}$'s are the projections of $\mathbf{w}_+ + \mathbf{w}_\times$ on their average vector. The analytic solutions for the other polarization constraints are straightforward to find, and we present them here. Such significant simplification of the inverse problem is possible due to the polarization transformations introduced in this paper. It enables rapid searches over the entire sky and reconstruction of source coordinates in real time.

E. Sky localization

As described in Sec. II B, the maximum likelihood and other coherent statistics are functions of the sky coordinates θ and ϕ. They are sensitive to the arrival time of a GW

TABLE I. The constraints on e (first column), ψ (second column), and the pattern vector (third column). The corresponding polarization states are shown in the last column.

e constraint	ψ constraint	Pattern constraint	Polarization state
⋯	⋯	⋯	r waves
$\mathrm{sign}(e[i]) = \mathrm{const}$	⋯	⋯	$\imath$ waves
⋯	$\psi[i] = \mathrm{const}$	⋯	ψ waves
$e[i] = \mathrm{const}$	$\psi[i] = \mathrm{const}$	⋯	Elliptical
$e[i] = 0$	$\psi[i] = \mathrm{const}$	⋯	Linear
⋯	⋯	$\tilde{\boldsymbol{\xi}}_\times = 0$	Loose linear
$e[i] = \pm 1$	⋯	⋯	Circular
⋯	⋯	$\boldsymbol{\xi}_\times = 0$	Loose circular

signal at the detector sites and can be used for the source localization. The reconstructed source location is defined at the maximum of the likelihood statistic $L_{\max}(\theta,\phi)$ or the sky statistic

$$L_{\mathrm{sky}}(\theta,\phi) = c_c(\theta,\phi) L_{\max}(\theta,\phi). \tag{3.14}$$

The L_{sky} statistic has better performance than $L_{\max}$ for networks with two detectors, and both statistics have comparable performance for larger networks. The probability distribution over the sky is calculated as

$$P_{\mathrm{sky}}(\theta,\phi) \propto (|\mathbf{f}_+|^2 + |\mathbf{f}_\times|^2)^n \exp\left[\frac{S - S_\circ}{2\sigma_s^2}\right], \tag{3.15}$$

where S is either $L_{\max}$ or L_{sky}, $S_\circ$ is the maximum of S in the sky, and σ_s is the scaling parameter close to unity.

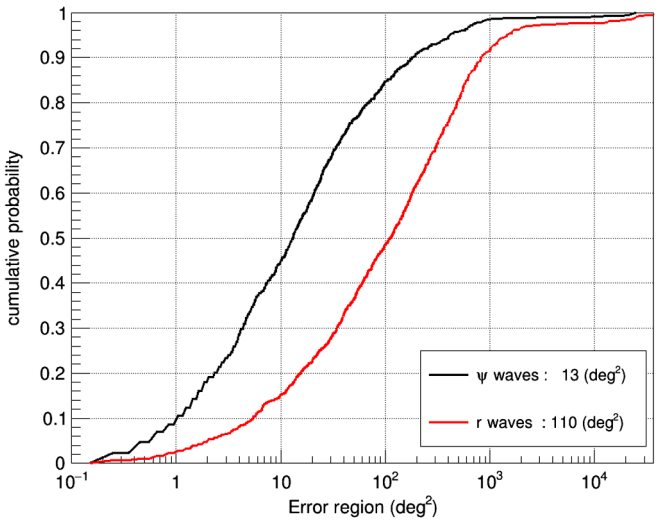

FIG. 3. Fraction of sources (vertical axis) reconstructed by the advanced Livingston-Hanford-Virgo network (at designed sensitivity) within the error region in square degrees (horizontal axis: the legend shows the median search area) for a simulated population of binary black holes: uniform in volume distribution with component masses between 15 and 25 solar mass and spin parameter between 0 and 0.9.

The parameter $n = 2$ invokes the antenna pattern prior function used for networks with two detectors. For $n = 0$, the prior is not used. The scaling parameter σ_s could vary depending on the network and used to calibrate the probability P_{sky}, so it correctly represents the fraction of sources found in a given error region. Figure 3 shows the sky localization performance of the advanced Livingston-Hanford-Virgo network for a population of simulated signals expected from mergers of compact binary sources. It is characterized by the median search area defined as the size of the error region in the sky containing 50% of sources. Also, Fig. 3 shows that the ψ-wave constraint significantly improves the source localization. This is an expected improvement for the sky localization constrained by the source models [27]. Of course, any modeled sky localization can be biased when the model does not accurately match the observation. However, the ψ-wave constraint uses a very general assumption about the compact binary sources, and no significant bias is expected.

IV. NETWORK CONSTRAINTS

The polarization constraints should be distinguished from the network constraints (or regulators), which give a model-independent way to constrain the wave parameters $h_o[i], \psi[i]$, and $e[i]$. The main purpose of the regulators is to eliminate unlikely solutions of the likelihood functional and, therefore, reduce the false alarm rates due to the instrumental and environmental artifacts in the data. The first network regulators were introduced by Klimenko *et al.* [25] to utilize the network properties in the likelihood analysis. Depending on the configuration, detector noise, and sky location, the detector network may have much lower sensitivity to the second GW component: $|\mathbf{f}_\times| \ll |\mathbf{f}_+|$. In this case, most of the network SNR is produced by the $\mathbf{f}_+$ response [see Eq. (2.8)]. The $\mathbf{f}_\times$ network response is likely to yield low SNR and, therefore, may not be reconstructed from the noisy data. Such *a priori* knowledge can be used in the analysis to constrain the likelihood solutions and reduce the number of free parameters in the wave model.

A. Network and event index

The weight of each detector in the network is defined by its noise-scaled response [Eq. (2.5)]. Depending on the spectral characteristics of the detector noise and the source sky location, the detector can be a key player in the network or just a spectator. The detector role varies from event to event and with time, depending on the run conditions. The quality of the network depends on how many detectors can contribute to the measurement. It is characterized by the network index

$$I_n = \frac{|\mathbf{f}_+|^2 + |\mathbf{f}_\times|^2}{|\mathbf{f}_+|^2 \nu(\mathbf{e}_+) + |\mathbf{f}_\times|^2 \nu(\mathbf{e}_\times)}, \tag{4.1}$$

where $\nu(\mathbf{e}) = \sum_k e_k^4$ for any unit vector $\mathbf{e}$. The network index is distributed between 1 and K representing the effective number of detectors available for the measurement. It is useful to introduce also the event index

$$I_e = \frac{|\boldsymbol{\xi}'|^2 + |\tilde{\boldsymbol{\xi}}'|^2}{|\boldsymbol{\xi}'|^2\nu(\mathbf{u}) + |\tilde{\boldsymbol{\xi}}'|^2\nu(\mathbf{v})}, \tag{4.2}$$

where the unit vectors $\mathbf{u}$ and $\mathbf{v}$ are along the OPT vectors $\boldsymbol{\xi}'$ and $\tilde{\boldsymbol{\xi}}'$, respectively (see Sec. III A). The event index represents the effective number of coincident detectors participating in the measurement. Usually, a low value of I_e or a significant difference between I_n and I_e is an indication of a spurious event produced by the detector noise.

Note, for calculation of the event index and the other coherent statistics, the reconstructed responses should be transformed to the OPT pattern $\{\boldsymbol{\xi}', \tilde{\boldsymbol{\xi}}'\}$, where the vectors $\mathbf{u}$ and $\mathbf{v}$ are orthogonal. They define the projection operators $P_{nm}(\mathbf{u})$ and $P_{nm}(\mathbf{v})$, respectively [see Eq. (2.15)]. The coherent statistics (2.11) and (2.12) are calculated individually for the 0°-phase and −90°-phase data and combined together.

B. Regulators

As prescribed by the unconstrained likelihood analysis, the orientation of the reconstructed response $\boldsymbol{\xi}$ is always along the unit vector $\mathbf{u}$ [see Eq. (2.16)]. However, when $|\mathbf{f}_\times| = 0$, which is the case for detectors with coaligned arms, the true network response must be pointing along the vector $\mathbf{f}_+$. Therefore, instead of the vector $\mathbf{u}$, the unity vector along $\mathbf{f}_+$ must be selected for the projection. This constitutes the hard regulator, which constrains the likelihood analysis to ignore the × response of the network. This and several other regulators have been used to analyze data collected by the initial LIGO and Virgo detectors.

Given a network of detectors, in some cases it is possible to predict the distributions of the wave parameters and anticipated network responses to a generic GW signal. The polarization transformation significantly simplifies the construction of regulators. After substituting the left side of Eqs. (3.10)–(3.12) with the data pattern vectors $\{\mathbf{w}_+, \mathbf{w}_\times, \tilde{\mathbf{w}}_\times\}$, we obtain the following identities

$$\alpha^2|\mathbf{w}_+|^2 = |\mathbf{f}_\times|^2 h_\circ^2 \beta_+^2(e,\gamma), \tag{4.3}$$

$$|\mathbf{w}_\times|^2 + |\tilde{\mathbf{w}}_\times|^2 = |\mathbf{f}_\times|^2 h_\circ^2 \beta_-^2(e,\gamma), \tag{4.4}$$

$$-\alpha(\mathbf{w}_\times \cdot \mathbf{e}_\times)|\mathbf{w}_+| = |\mathbf{f}_\times|^2 h_\circ^2 \frac{1-e^2}{2}\sin(2\gamma), \tag{4.5}$$

$$\alpha(\tilde{\mathbf{w}}_\times \cdot \mathbf{e}_\times)|\mathbf{w}_+| = |\mathbf{f}_\times|^2 h_\circ^2 e \tag{4.6}$$

that can be solved for e and $\sin(\gamma)$. As prescribed by Eqs. (3.11) and (3.12), the responses $\boldsymbol{\xi}_\times$ and $\tilde{\boldsymbol{\xi}}_\times$ vanish when $\sin(\gamma) \to 0$ and $e \to 0$, respectively. Figure 4 shows the distributions of the reconstructed e and $\sin(\gamma)$ for the noise and signal, and the Livingston-Hanford network. Unlike the signal, the noise is clustering at low values of e and $\sin(\gamma)$. The noisy data can be identified by the regulator

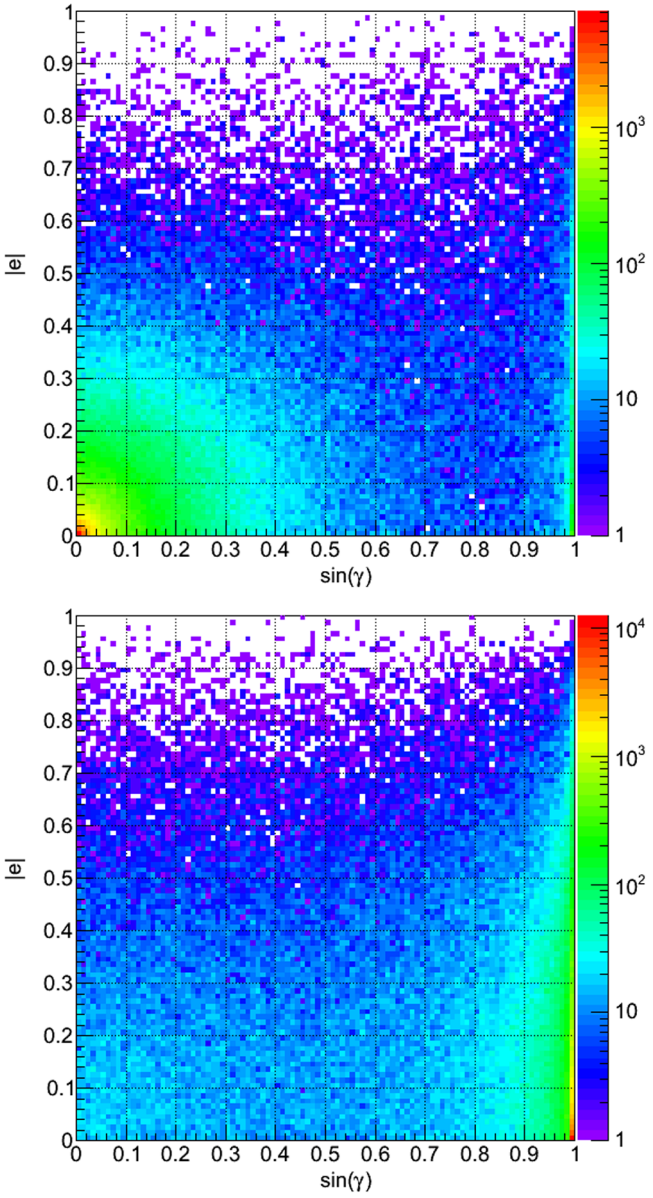

FIG. 4. Distribution of e and $\sin(\gamma)$ for the Livingston-Hanford network obtained from the simulation of a single-pixel events uniformly distributed over the sky. The top plot is for Gaussian noise, and the bottom plot is for the signal with the random polarization.

$$\Gamma = \sqrt{e^2 + \sin^2(\gamma)} \tag{4.7}$$

when Γ is below some threshold Γ_o. For appropriately selected Γ_o, the regulator identifies data pixels with the marginal signal components $\boldsymbol{\xi}_\times$ and $\tilde{\boldsymbol{\xi}}_\times$ and zeroes them. The regulated responses ($\boldsymbol{\xi}_+ = \mathbf{w}_+$, $\boldsymbol{\xi}_\times = 0$, $\tilde{\boldsymbol{\xi}}_\times = 0$) are

biased: a small fraction of events can be misreconstructed and excluded from the analysis. Despite this relatively small (and controlled) loss, the regulator otherwise is very efficient in reducing the false alarm rates (FAR) due to spurious events, with a typical reduction factor of $\sim 10^{-6}$. It entirely eliminates the single detector FAR and significantly suppresses FAR from the accidental coincident events produced by the detector pairs. To further reduce the double coincidence FAR, we introduce the second regulator, which utilizes the network and the event indexes

$$\Delta = I_e^{-1} - \alpha|\nu(\mathbf{e}_+) - \nu(\mathbf{e}_\times)|. \tag{4.8}$$

The condition $\Delta > 0.5$ is used to identify the situation when two or fewer detectors are used in the measurement. In this case, the reconstructed responses are constrained to be ($\boldsymbol{\xi}_+ = \mathbf{w}_+$, $\boldsymbol{\xi}_\times = 0$, $\tilde{\boldsymbol{\xi}}_\times = \tilde{\mathbf{w}}_\times$). Both regulators can be used to constrain the detector networks when either the network alignment coverage is insufficient or the effective number of detectors is fewer than two.

V. CONCLUSION

In this paper, we present the improved analytic framework of the CWB analysis algorithm. The objective of this analysis is the detection and reconstruction of unmodeled GW transients. It is achieved by solving the burst inverse problem—reconstruction of the signal waveforms, wave polarization, and the sky coordinates of the source. The reconstruction is performed by using the likelihood formalism with the signal waveforms as free parameters. The waveforms can be described with the wave parameters and constrained, which enable a range of weakly modeled burst searches. The likelihood analysis yields a number of detection statistics used for the ranking of detected events (the network coherent SNR), the rejection of background events (the network correlation coefficient), and for the sky localization.

The novelty of this paper is in the introduction of the polarization patterns. By imposing a simple phase transformation to the network data, a characteristic pattern emerges revealing the polarization state of an arbitrary GW signal. This unique signature of the signal can be measured independently from the other source parameters. The polarization transformation significantly simplifies the solution of the inverse problem: the detector responses can be reconstructed directly from the pattern. The polarization constraints can be imposed, which enable weakly modeled burst searches. The reconstruction is computationally efficient allowing for rapid searches over the entire sky and the reconstruction of source coordinates in real time with a few minutes latency. We also identify factors limiting reconstruction and how the polarization measurements are affected by the network. A simple metric (network alignment factor α) determines the network ability to capture polarizations. The network of LIGO and Virgo detectors has a low alignment coverage for a significant fraction of the sky. Therefore, in most cases, the polarization state of a weak GW signal cannot be measured. Adding Kagra and LIGO-India detectors to the advanced network will significantly improve the alignment coverage and, hence, the reconstruction of the signal parameters.

ACKNOWLEDGMENTS

We are thankful to the National Science Foundation for support under Grants No. PHY 1205512 and No. PHY 1505308. This document has been assigned LIGO Laboratory Document No. P1500206.

[1] B. P. Abbott *et al.*, Classical Quantum Gravity **32**, 074001 (2015).
[2] F. Acernese *et al.* (Virgo Collaboration), Classical Quantum Gravity **32**, 024001 (2015).
[3] http://gwcenter.icrr.u-tokyo.ac.jp/en/.
[4] https://dcc.ligo.org/LIGO-M1100296/public.
[5] J. Abadie *et al.*, Classical Quantum Gravity **27**, 173001 (2010).
[6] S. Klimenko, I. Yakushin, A. Mercer, and G. Mitselmakher, Classical Quantum Gravity **25**, 114029 (2008).
[7] P. J. Sutton, G. Jones, S. Chatterji, P. Kalmus, I. Leonor, S. Poprocki, J. Rollins, A. Searle, L. Stein, and M. Tinto, New J. Phys. **12**, 053034 (2010).
[8] E. Thrane *et al.*, Phys. Rev. D **83**, 083004 (2011).
[9] R. Lynch, S. Vitale, R. Essick, and E. Katsavounidis, arXiv:1511.05955.
[10] J. Abadie *et al.* (LIGO Scientific and VIRGO Collaborations), Astron. Astrophys. **539**, A124 (2012).
[11] J. Aasi *et al.* (LIGO Scientific and VIRGO Collaborations), Astrophys. J. Suppl. Ser. **211**, 7 (2014).
[12] B. D. Metzger and E. Berger, Astrophys. J. **746**, 48 (2012).
[13] C. Pankow, S. Klimenko, G. Mitselmakher, I. Yakushin, G. Vedovato, M. Drago, R. A. Mercer, and P. Ajith, Classical Quantum Gravity **26**, 204004 (2009).
[14] J. Abadie *et al.* (The LIGO Scientific Collaboration and The Virgo Collaboration), Phys. Rev. D **81**, 102001 (2010).
[15] J. Abadie *et al.* (LIGO Scientific Collaboration, Virgo Collaboration), Phys. Rev. D **85**, 102004 (2012).
[16] J. Abadie *et al.* (The LIGO Scientific Collaboration and The Virgo Collaboration), Phys. Rev. D **85**, 122007 (2012).
[17] J. Aasi *et al.* (LIGO Scientific Collaboration, Virgo Collaboration), Phys. Rev. D **89**, 122003 (2014).

[18] S. Klimenko, G. Vedovato, M. Drago, G. Mazzolo, G. Mitselmakher, C. Pankow, G. Prodi, V. Re, F. Salemi, and I. Yakushin, Phys. Rev. D **83**, 102001 (2011).
[19] V. Necula, S. Klimenko, and G. Mitselmakher, J. Phys. Conf. Ser. **363**, 012032 (2012).
[20] V. Tiwari *et al.*, Classical Quantum Gravity **32**, 165014 (2015).
[21] V. Tiwari, S. Klimenko, V. Necula, and G. Mitselmakher, Classical Quantum Gravity **33**, 01LT01 (2016).
[22] R. Essick, S. Vitale, E. Katsavounidis, G. Vedovato, and S. Klimenko, Astrophys. J. **800**, 81 (2015).
[23] Y. Gürsel and M. Tinto, Phys. Rev. D **40**, 3884 (1989).
[24] É. E. Flanagan and S. A. Hughes, Phys. Rev. D **57**, 4566 (1998).
[25] S. Klimenko, S. Mohanty, M. Rakhmanov, and G. Mitselmakher, Phys. Rev. D **72**, 122002 (2005).
[26] S. D. Mohanty, M. Rakhmanov, S. Klimenko, and G. Mitselmakher, Classical Quantum Gravity **23**, 4799 (2006).
[27] L. P. Singer *et al.*, Astrophys. J. **795**, 105 (2014).